

# Mixing model of Phobos' bulk elemental composition for the determination of its origin: Multivariate analysis of MMX/MEGANE data

Kaori Hirata<sup>a,b,\*</sup>, Tomohiro Usui<sup>a</sup>, Ryuki Hyodo<sup>a</sup>, Hidenori Genda<sup>c</sup>, Ryota Fukai<sup>a</sup>, David J. Lawrence<sup>d</sup>, Nancy L. Chabot<sup>d</sup>, Patrick N. Peplowski<sup>d</sup>, Hiroki Kusano<sup>e</sup>

<sup>a</sup>*Institute of Space and Astronautical Science (ISAS), Japan Aerospace Exploration Agency (JAXA), 3-1-1 Yoshinodai, Sagami-hara, Kanagawa 2525210, Japan*

<sup>b</sup>*Department of Earth and Planetary Science, The University of Tokyo, 7-3-1 Hongo, Bunkyo, Tokyo 1130033, Japan*

<sup>c</sup>*Earth-Life Science Institute (ELSI), Tokyo Institute of Technology, 2-12-1 Ookayama, Meguro, Tokyo, 1528550, Japan*

<sup>d</sup>*The Johns Hopkins University Applied Physics Laboratory, Laurel, MD 20723, USA*

<sup>e</sup>*National Institutes for Quantum Science and Technology, 4-9-1 Anagawa, Inage, Chiba 2638555, Japan*

---

## Abstract

The formation process of the two Martian moons, Phobos and Deimos, is still debated with two main competing hypotheses: the capture of an asteroid or a giant impact onto Mars. In order to reveal their origin, the Martian Moons eXploration (MMX) mission by Japan Aerospace Exploration Agency (JAXA) plans to measure Phobos' elemental composition by a gamma-ray and neutron spectrometer called MEGANE. This study provides a model of Phobos' bulk elemental composition, assuming the two formation hypotheses. Using the mixing model, we established a MEGANE data analysis flow to discriminate between the formation hypotheses by multivariate analysis. The mixing model expresses the composition of Phobos in 6 key lithophile elements that will be measured by MEGANE (Fe, Si, O, Ca, Mg, and Th) as a linear mixing of two mixing components: material from Mars and material from an asteroid as represented by primitive meteorite compositions. The inversion calculation includes consideration of MEGANE's measurement errors ( $E_P$ ) and derives the mixing ratio for a given Phobos composition, based on which the formation hypotheses are judged. For at least 65% of the modeled compositions, MEGANE measurements will determine the origin uniquely ( $E_P = 30\%$ ), and this increases from 74 to 87% as  $E_P$  decreases from 20 to 10%. Although the discrimination performance depends on  $E_P$ , the current operation plan for MEGANE predicts an instrument performance for  $E_P$  of 20–30%, resulting in 70% discrimination between

---

\*Corresponding author

*Email address:* hirata-kaori444@g.ecc.u-tokyo.ac.jp (Kaori Hirata)

the original hypotheses. MEGANE observations can also enable the determination of the asteroid type of the captured body or the impactor. The addition of other measurements, such as MEGANE’s measurements of the volatile element K, as well as observations by other MMX remote sensing instruments, will also contribute to the MMX mission’s goal to constrain the origin of Phobos.

*Keywords:* Martian moons, Phobos, formation hypothesis, MMX, MEGANE, elemental composition

---

## 1. Introduction

The study of the Mars-moons system is crucial for understanding the initial environment of Mars as seen in the studies of the Earth-Moon system. The Martian moons, Phobos and Deimos, have been studied by telescope observations or remote sensing by Mars exploration missions. However, the origin of the Martian moons still remains controversial with two leading hypotheses.

One leading hypothesis is the capture of an asteroid, where an asteroid formed some distance from Mars and was captured by the gravity of Mars to become a satellite. This hypothesis is mainly supported by the similarity of surface characteristics (Pollack (1977); Thomas et al. (1992)) and surface spectra (Burns (1978); Burns (1992); Pajola et al. (2013); Pollack et al. (1979)) between the Martian moons and main-belt asteroids. The surface spectra of Phobos and Deimos are characterized by their low albedo and spectral properties similar to D-type asteroids that lack a diagnostic absorption band (Murchie et al. (1991); Pang et al. (1978); Pollack et al. (1978); Rivkin (2002)). In contrast to the spectral similarity, the observed orbital properties of Phobos and Deimos are difficult to account for by the capture origin. The capture origin predicts a high eccentricity and high inclination of the moons’ initial orbits, which is inconsistent with the present orbits of the Martian moons (Safronov & Ruskol (1977)). Numerical models have examined the processes to change their orbits after the gravitational capture by Mars (Burns (1992); Cazenave et al. (1980); Craddock (1994); Craddock (2011); Hunten (1979); Lambeck (1979); Szeto (1983); Rosenblatt (2011)), but neither of them successfully reconstructed their orbits completely.

The second hypothesis is the in-situ formation from a circum-Martian disk produced by a giant impact. This scenario is consistent with the near-circular and near-equatorial orbits of Phobos and Deimos (Canup & Salmon (2018); Citron et al. (2015); Craddock (2011); Hesselbrock & Minton (2017); Hyodo et al. (2017a); Hyodo et al. (2017b)). The disk materials and the resultant Martian moons are expected to consist of both the impactor material and the ejecta launched from Mars by the giant impact (Pignatale et al. (2018); Hyodo et al. (2017b)). The thermophysical property of disk materials depends on the impact condition, such as the impactor size and velocity. Moreover, the giant impact hypothesis predicts the depletion of volatile elements due to the impact heating (Craddock (2011); Hyodo et al. (2017b); Nakajima & Stevenson (2018); Pignatale et al. (2018)).

Other hypotheses have been proposed for the Martian moons as well, such as in-situ formation from a debris disk around Mars with the moons forming as second-generation objects (Pätzold et al. (2014)). Bagheri et al. (2021) proposed a hypothesis that a single Martian moon was tidally disrupted and split into two moons although Hyodo et al. (2022) later theoretically investigated the orbital evolution and argued that two moons that originated by splitting from a common parent body were likely to be disrupted by collisions, which is inconsistent with the existence of the current Martian moons. The compositions expected for these scenarios are similar to the main two hypotheses, depending on if the material in the debris disk or disrupted body derived fundamentally from a captured object or from Martian material. Thus, determining between these two compositional endmembers is key for determining the origin of the Martian moons.

Bulk elemental compositions reflect the moons' formation processes and potentially discriminate them. The bulk composition is estimated as chondritic for the capture scenario, whereas it represents a mixture of chondritic and Martian materials for the impact scenario (Hyodo et al. (2017b); Pignatale et al. (2018)). While the surface composition of the Martian moons likely experienced some post-formation modifications due to processes, such as late accretion and space weathering, the bulk composition could have survived those processes and preserved the original information of the building blocks (Hyodo et al. (2019); Ramsley & Head (2013a); Ramsley & Head (2013b); Ramsley & Head (2017)).

Japan Aerospace Exploration Agency (JAXA) is planning the Martian moons' sample return mission (MMX: Martian Moons eXploration) (Kawakatsu et al. (2023); Kuramoto et al. (2022); Usui et al. (2020); Nakamura et al. (2021)). MMX has two major science goals: 1) to reveal the origin of Martian moons and gain a better understanding of the planetary formation and material transport in the solar system, and 2) to observe processes that have an impact on the evolution of the Mars system. To achieve these goals, MMX will conduct comprehensive mineralogical (visible to near IR imaging), geochemical (elemental abundances), and geophysical (shape and gravity) measurements by seven science payloads and analyses of returned samples of Phobos (Kuramoto et al. (2022); Nakamura et al. (2021)).

Among the MMX science payload is the Mars-moon Exploration with Gamma rays and NEutrons (MEGANE) instrument (Lawrence et al. (2019)). MEGANE will use gamma-ray and neutron spectroscopy to measure the elemental composition of Phobos from orbit. By detecting gamma-rays with specific energies and neutron fluxes, MEGANE will measure the abundance of major and minor elements (e.g., O, Si, Mg, Ca, and Fe), radioactive elements (e.g., K, Th, and U), and light elements (e.g., H) on the top  $\sim 30$ cm of the surface of Phobos; Measurements by OROCHI (Optical RadiOmeter composed of CHromatic Imagers; Kameda et al. (2021)) and MIRS (MMX InfraRed Spectrometer; Barucci et al. (2021)), which are other MMX payload instruments, will provide mineralogical and geophysical information by investigating the topmost surface ( $\sim 1\mu\text{m}$ ) of Phobos. Thus, MEGANE observations are expected to reveal the composition of Phobos' near-surface materials and be complemented by observations by

other MMX instruments.

The elemental composition acquired by MEGANE will provide insights into the formation scenario of the Martian moons. The large spatial footprints of MEGANE will be combined to determine Phobos' average surface composition, revealing the bulk elemental composition of Phobos. Note that MEGANE's observation error depends on the observation conditions, such as the accumulation period and the orbital altitude during the observations (Chabot et al. (2021); Lawrence et al. (2019)). Peplowski (2016) previously suggested that observations at one target-body radius for more than 10 days are needed to obtain adequate signal-to-background. Since the composition of Phobos reflects both a formation process and the evolutionary conditions experienced by the materials (e.g., the composition of building blocks and/or thermophysical properties in the impact-induced disk), the accurate interpretation of MEGANE data to confine the formation scenario (i.e., capture versus impact) requires a comprehensive investigation under a wide range of parameters that consider the endmember compositions as well as their mixing ratios.

This study aims to establish an elemental composition model of the Martian moons applicable to interpreting the MEGANE data to discriminate among the proposed origins of the Martian moons. We constructed a mixing model of the elemental composition of the Martian moons assuming the mixing of end-components of chondritic and Martian compositions. Consideration of several types of errors were included and revealed the relationship between the plausible formation scenarios and the ability of MEGANE data to discriminate among the hypotheses. Using this model, we investigated MEGANE's discrimination performance as applied to the two main formation hypotheses for the Martian moons.

## 2. Method

This study constructed a model for Phobos' elemental composition that connects the formation scenarios proposed and the elemental composition that will be measured by MEGANE assuming a mixture of the two end-components of Martian and asteroidal materials (Fig. 1). First, the forward-solving approach, which predicts the composition from each origin scenario, is introduced (Section 2.1). Second, the inverse-solving approach to discriminate among the origin scenarios from MEGANE measurements is shown (Section 2.2). Finally, we define the discrimination performance to evaluate MEGANE's ability to distinguish among the origin hypotheses and investigate the dependency on parameters that are related to MEGANE's operations and measurements (Section 2.3).

### *2.1. Mixing Model: Forward-solving Approach*

#### *2.1.1. Concept*

We defined the mixing model for the composition of Phobos based on the two main formation hypotheses (Fig. 2). The composition of Phobos was expressed as representing a two-component mixture with a certain mixing ratio

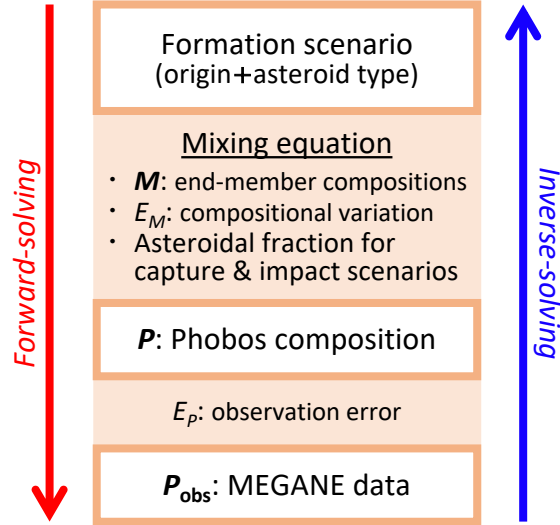


Figure 1: The forward- and inverse-solving approaches using the mixing model. This model connects the formation scenarios of Phobos and the elemental composition that will be measured by MMX MEGANE.

( $r\%$ ) between the Martian composition ( $100 - r\%$ ) and an asteroid composition ( $r\%$ ). Note that  $r = 100\%$  in the case of the capture origin and can be a range of values between  $0\%$  and  $100\%$  in the case of the impact origin. This model *forwardly* predicted Phobos' composition and measurements that would be obtained from MEGANE's observation data for a given formation scenario (formation hypothesis + asteroid type).

### 2.1.2. Parameters and Assumptions

To illustrate a variety of Phobos' origin scenarios, our model used 3 parameters: the composition of mixing end-members, the modeled asteroidal fraction for capture and impact origins, and the MEGANE's observation error.

*The composition of mixing end-members.* Meteorite data were used for the mixing end-member compositions using Martian and asteroidal compositions (Table 1). For the Mars component, a composition for a silicate portion (Bulk Silicate Mars, BSM; Taylor (2013)) was assumed in our model. This is based on the calculation by Hyodo et al. (2017b) which indicated that the Martian ejecta in the impact origin scenarios would mainly come from a depth where both the crust and mantle were included and the compositions were not dominated by the crustal portion alone. Nevertheless, we would like to note that consideration of the diversity of crustal composition on Mars (e.g., Hahn et al. (2007)) did not change our results because variations among Martian compositions are relatively

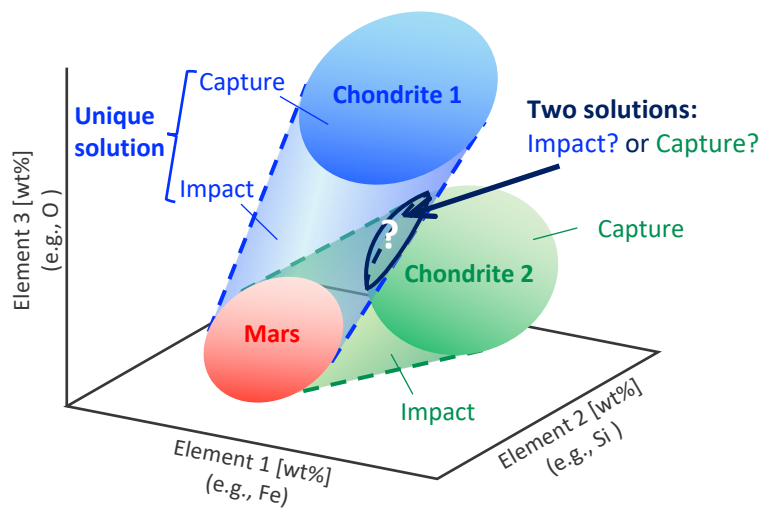


Figure 2: A schematic of the mixing model for Phobos' elemental composition. Spheroids represent end-member compositions with compositional variations (red: Martian composition, blue and green: asteroidal composition). In the case of a capture origin, Phobos' composition is modeled as that of the captured asteroid composition (i.e., within the blue or green spheres). On the other hand, in the case of an impact origin, Phobos' composition should be an intermediate composition between Mars and an asteroid (i.e., between the two red and blue or green spheres).

small compared with the compositional differences among Mars and asteroidal compositions. For the asteroid end-members, chondritic compositions that are considered to correspond to major components of main-belt asteroids (DeMeo & Carry (2014); Gradie & Tedesco (1982)), i.e., S-, C-, E-, and D-type asteroids, were applied (Table 1). Chondrites are traditionally classified into 3 groups, Carbonaceous Chondrite (CC), Ordinary Chondrite (OC), and Enstatite Chondrite (EC) (Brearley et al. (1998)). Each class is further composed of several groups. In this study, elemental abundances of eleven chondrite groups with primitive compositions and one ungrouped chondrite with a composition similar to D-type asteroids (Alexander (2019b); Alexander (2019a)) were used: 6 CCs (CI, CM, CO, CV, CK, and CR), 3 OCs (H, L, and LL), 2 ECs (EH and EL), and 1 ungrouped (Tagish Lake) (Table 1).

MEGANE can measure the abundance of major elements (e.g., Fe, Si, O, Ca, and Mg) and radioactive elements (e.g., K and Th) (Lawrence et al. (2019)). This study followed the element classification adopted by Taylor (2013), in which Fe, Si, O, Ca, Mg, and Th are referred to as lithophile elements and K is classified as a moderately volatile element. Among these elements, we selected 6 lithophile elements to model Phobos' composition. In Section 4.4.3, we discuss the use of K abundance as well.

Additionally, this study took into account the end-members' compositional variations and introduced a relative error of 10%.

	BSM <sup>a</sup>	CI <sup>b</sup>	CM <sup>b</sup>	CO <sup>b</sup>	CV <sup>b</sup>	CK <sup>b</sup>	CR <sup>b</sup>	H <sup>c</sup>	L <sup>c</sup>	LL <sup>c</sup>	EH <sup>c</sup>	EL <sup>c</sup>	TL <sup>b</sup>
Fe [wt%]	14.1	18.5	21.2	24.7	23.6	23.4	24.1	27.5	21.5	18.5	29.0	22.0	18.9
Si [wt%]	20.5	10.7	13.0	16.0	16.0	15.9	15.8	16.9	18.5	18.9	16.7	18.6	11.6
O [wt%]	42.0	45.9	40.4	35.1	36.7	37.0	36.8	32.9	36.3	37.7	28.1	33.0	37.9
Ca [wt%]	1.74	0.91	1.24	1.56	1.85	2.00	1.38	1.25	1.31	1.30	0.85	1.08	0.99
Mg [wt%]	18.5	9.5	11.7	14.4	14.8	14.8	13.9	14.0	14.9	15.3	10.6	14.1	10.9
Th [ppb]	5.8	3.0	3.9	4.5	6.3	5.8	4.2	4.2	4.3	4.3	3.0	3.4	3.8

Table 1: The elemental composition of 6 elements (Fe, Si, O, Ca, Mg, and Th) for the 13 end-members (Mars (BSM); Bulk Silicate Mars), 6 CCs, 3 OCs, 2 ECs, and ungrouped (TL; Tagish Lake)) assumed in the model.

<sup>a</sup>: Taylor (2013), <sup>b</sup>: Alexander (2019a), <sup>c</sup>: Alexander (2019b)



*Modeled asteroidal fraction for capture and impact origins.* In the case of the asteroid capture hypothesis, the elemental composition of Phobos is similar to that of a captured asteroid. In this case, our model assumed that Phobos’ building blocks are composed only of the material from the captured asteroid, resulting in an asteroidal fraction of 100%.

On the other hand, in the giant impact hypothesis, the fraction of impactor material (i.e., modeled asteroidal fraction) varies depending on the impact condition, such as the size of the impactor or the impact angle and velocity (e.g., Canup & Salmon (2018); Hyodo et al. (2017b)). Using numerical simulations, Hyodo et al. (2017b) investigated the thermophysical properties of the impact-induced disk from which the Martian moons formed. They suggested that the building blocks of Phobos should contain both Martian materials of  $\gtrsim 50\%$  and impactor materials of  $\gtrsim 35\%$ , while the mixing ratio changes depending on the impact conditions, e.g., impact velocity or angle. For example, disk materials are composed of 40% Martian materials and 60% impactor materials to form the Borealis basin on Mars with an impactor mass of 0.03 times that of Mars and an impact angle of  $45^\circ$ . Considering that Phobos and Deimos accreted in the outer part of the impact-induced disk (Rosenblatt et al. (2016)), 70% of the outer disk material was estimated to come from Mars. It was also suggested that the mixing ratio of impactor material would also depend on the impact angle, changing the mixing ratio from 30% to 65%. As a reference, this study assumed the modeled asteroidal fraction of 50% for impact origin (reference case), which means that a giant impact results in a mixing of 50% asteroidal materials and 50% Martian materials. More practically, the uncertainty of mixing conditions was taken into account and the modeled asteroidal fraction of 30–70% was adopted for the impact origin (practical case).

*MEGANE observation error.* The observation error of MEGANE depends on the observation sequence, especially the accumulation period and the orbital altitude. Peplowski (2016) previously suggested that gamma-ray and neutron measurements require orbital altitudes less than or equal to 1-target body radius for successful analysis. Lawrence et al. (2019) estimated the observation error needed to meet the MEGANE science objectives element by element and determined that this error could be achieved with at least 10 days of accumulation at altitudes equal to or less than 1-target body radius. We assumed 30, 20, 10, and 0% relative error for the MEGANE observation error in our model calculations:  $E_P = 30, 20, 10, \text{ and } 0$  [%].

### 2.1.3. Mixing Equation

Our mixing model calculated the composition of Phobos as a linear sum of Martian and asteroidal compositions, with a certain mixing ratio. Phobos’ composition ( $\mathbf{P}$ ) resulting from the mixing of the compositions of Mars ( $M_0$ ) and an asteroid  $i$  ( $M_i$ ;  $i = 1, 2, \dots, 12$ ) was expressed by Eq. 1, using matrices  $\mathbf{P}$ ,  $\mathbf{M}$ , and  $\mathbf{R}$ .  $\mathbf{P}$  represented the abundance of 6 elements on Phobos: Fe, O, Si, Ca, Mg, and Th. The end-member composition matrix  $\mathbf{M}$  was composed of the same 6-element composition of Mars ( $M_0$ ) and asteroids ( $M_i$ ;  $i = 1, 2, \dots, 12$ ),

$\mathbf{M} = [M_0 M_1 \cdots M_{12}]$ . The mixing ratio matrix  $\mathbf{R}$  was composed of the mixing ratios for  $i$ -th end-member compositions ( $r_i$ ;  $i = 0, 1, 2, \dots, 12$ ). Note that since we assumed the mixing of only two end-components, i.e., Mars and the selected type of asteroid  $i'$ ,  $r_i = 0$  for  $i \neq i'$  and  $r_0 = 1 - r_{i'}$ . The abundance of each element ( $P_e$ ;  $e = \text{Fe, O, Si, Ca, Mg, and Th}$ ) in Phobos' material was written down using that in Mars ( $M_{e,0}$ ) and asteroid ( $M_{e,i}$ ) materials and the mixing ratio  $r_i$ . The subscript  $e$  indicates the type of elements (Fe, O, Si, Ca, Mg, and Th), and  $i$  indicates the mixing end-members (Martian component for  $i = 0$  and asteroids for  $i = 1-12$ ).

$$\mathbf{P} = \mathbf{M}\mathbf{R},$$

$$\begin{pmatrix} P_{\text{Fe}} \\ P_{\text{O}} \\ P_{\text{Si}} \\ P_{\text{Ca}} \\ P_{\text{Mg}} \\ P_{\text{Th}} \end{pmatrix} = \begin{pmatrix} M_{\text{Fe},0} & M_{\text{Fe},1} & \cdots & M_{\text{Fe},12} \\ M_{\text{O},0} & M_{\text{O},1} & \cdots & M_{\text{O},12} \\ M_{\text{Si},0} & M_{\text{Si},1} & \cdots & M_{\text{Si},12} \\ M_{\text{Ca},0} & M_{\text{Ca},1} & \cdots & M_{\text{Ca},12} \\ M_{\text{Mg},0} & M_{\text{Mg},1} & \cdots & M_{\text{Mg},12} \\ M_{\text{Th},0} & M_{\text{Th},1} & \cdots & M_{\text{Th},12} \end{pmatrix} \begin{pmatrix} r_0 \\ r_1 \\ \vdots \\ r_i \\ \vdots \\ r_{11} \\ r_{12} \end{pmatrix}. \quad (1)$$

Considering relative errors  $E_P$  for  $\mathbf{P}$  and  $\mathbf{M}$  for  $E_M$ ,  $\mathbf{P}_{\text{obs}}$  and  $\mathbf{M}$  should be included in the range of  $[\mathbf{P}_{\text{obs,min}} : \mathbf{P}_{\text{obs,max}}]$  and  $[\mathbf{M}_{\text{min}} : \mathbf{M}_{\text{max}}]$ , respectively, which were given as

$$\mathbf{P}_{\text{obs,min}} = (P_{\text{obs,min},e}) = \mathbf{P} \times \frac{100 - E_P}{100}, \quad (2)$$

$$\mathbf{P}_{\text{obs,max}} = (P_{\text{obs,max},e}) = \mathbf{P} \times \frac{100 + E_P}{100}, \quad (3)$$

$$\mathbf{M}_{\text{min}} = (M_{\text{min},e,i}) = \mathbf{M} \times \frac{100 - E_M}{100}, \quad (4)$$

$$\mathbf{M}_{\text{max}} = (M_{\text{max},e,i}) = \mathbf{M} \times \frac{100 + E_M}{100}. \quad (5)$$

## 2.2. Discrimination of the Origin: Inverse-solving Approach

The *inverse-solving* approach uses our model to determine the origin of Phobos from its composition by using MEGANE data. First, a given composition was deconvolved into two mixing end components. The inverse calculation derived the mixing ratio  $r$  (Section 2.2.1; Fig. 3(a)). Next, the derived mixing ratio judged whether the formation scenarios were possible to explain the composition or not, based on the criteria (Section 2.2.2; Fig. 3(b)). By summarizing the judgments for all asteroid types, the composition was classified into 4 cases (Section 2.2.3; Fig. 3(c)).

### 2.2.1. Mixing ratio calculation

The mixing ratio for a given MEGANE compositional determination and a given asteroid type was derived from inverse calculations of the mixing equation (Eq. 1). The mixing ratio for each element  $r_{e,i}$  was determined. Since we

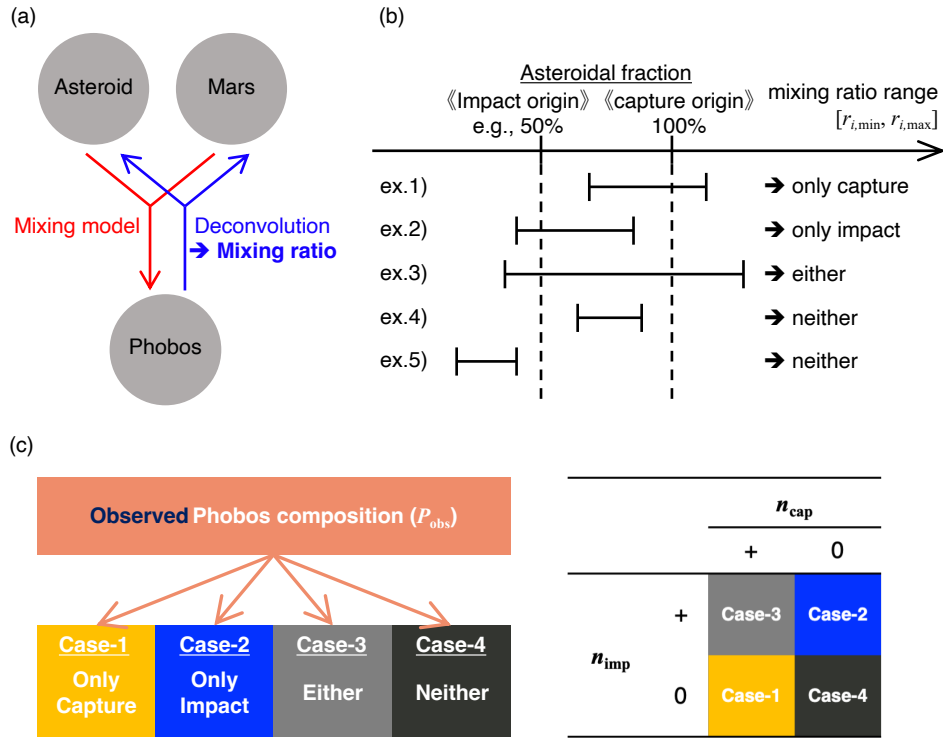


Figure 3: Schematics showing 3 calculation steps in the inverse-solving approach. (a) The observed Phobos composition is deconvolved into two mixing end-members. The mixing ratio is calculated (Section 2.2.1). (b) Formation hypotheses are judged based on whether the derived mixing ratio range agrees with the modeled asteroidal fraction for capture and impact origins. These calculations are performed on all types of asteroid compositions independently (Section 2.2.2). (c) By summarizing the judgments for all the asteroid types, a given Phobos composition measured by MEGANE is classified into 4 cases (Section 2.2.3).

assumed the MEGANE observation error  $E_P$ , the error for  $\mathbf{P}$ , and the compositional variation of Mars and asteroids  $E_M$ , the error for  $\mathbf{M}$ , the minimum and maximum values of  $r_{e,i}$  ( $r_{e,i,\min}$  and  $r_{e,i,\max}$ ) were calculated as

$$r_{e,i,\min} = \begin{cases} \frac{M_{\min,e,0} - P_{\text{obs,max},e}}{M_{\max,e,0} - M_{\max,e,i}} & (M_{e,0} \leq M_{e,i}), \\ \frac{M_{\min,e,0} - P_{\text{obs,min},e}}{M_{\min,e,0} - M_{\min,e,i}} & (M_{e,0} \geq M_{e,i}), \end{cases} \quad (6)$$

$$r_{e,i,\max} = \begin{cases} \frac{M_{\max,e,0} - P_{\text{obs,min},e}}{M_{\min,e,0} - M_{\min,e,i}} & (M_{e,0} \leq M_{e,i}), \\ \frac{M_{\max,e,0} - P_{\text{obs,max},e}}{M_{\max,e,0} - M_{\max,e,i}} & (M_{e,0} \geq M_{e,i}). \end{cases} \quad (7)$$

Note that  $\mathbf{P}$  represented the Phobos composition measured by MEGANE  $\mathbf{P}_{\text{obs}}$  in the inverse approach.

From the derived set of the mixing ratio range  $[r_{e,i,\min}, r_{e,i,\max}]$  for element  $e$  within 6 elements, we considered the common range among the 6 elements  $[r_{i,\min}, r_{i,\max}]$  as a possible solution for a given set of MEGANE observation data  $\mathbf{P}_{\text{obs}}$  and a given asteroid type  $i$ , as

$$[r_{i,\min}, r_{i,\max}] = [\max_{e=1,6} [r_{e,i,\min}], \min_{e=1,6} [r_{e,i,\max}]], \quad (8)$$

when  $\max_{e=1,6} [r_{e,i,\min}] \leq \min_{e=1,6} [r_{e,i,\max}]$ . Otherwise  $[r_{i,\min}, r_{i,\max}]$  would not have a solution.

### 2.2.2. Criteria for capture/impact hypothesis

The derived mixing ratio range  $[r_{i,\min}, r_{i,\max}]$  was used to judge the origin based on the modeled asteroidal fractions for the two formation hypotheses (Section 2.1.2; Fig. 3(b)). When the modeled asteroidal fraction is sandwiched between the derived mixing ratio range, the  $\mathbf{P}_{\text{obs}}$  was explained by the scenario:  $\mathbf{P}_{\text{obs}}$  could be explained by the capture and giant impact of asteroid  $i$  if the modeled asteroidal fraction for capture origin (100%) and impact origin (e.g., 50% in reference case) is sandwiched between  $[r_{i,\min}, r_{i,\max}]$ , respectively.

### 2.2.3. Classification based on the reasonable formation scenario

Based on the origin judgments, we counted the number of asteroid types ( $n_{\text{cap}}$  and  $n_{\text{imp}}$ ) that accounted for the  $\mathbf{P}_{\text{obs}}$  in the capture and impact origins, respectively (Fig. 3(c)). Then  $\mathbf{P}_{\text{obs}}$  was classified into 4 cases: (Case-1) in case  $n_{\text{cap}} > 0$  and  $n_{\text{imp}} = 0$ , only the capture hypothesis can explain a given  $\mathbf{P}$ , (Case-2) in case  $n_{\text{cap}} = 0$  and  $n_{\text{imp}} > 0$ , only the impact hypothesis can explain a given  $\mathbf{P}$ , (Case-3) in case  $n_{\text{cap}} > 0$  and  $n_{\text{imp}} > 0$ , either of the two hypotheses can explain a given  $\mathbf{P}$ , and (Case-4) in case  $n_{\text{cap}} = 0$  and  $n_{\text{imp}} = 0$ , neither hypothesis can explain a given  $\mathbf{P}$ . Under this definition, we can say that the origins of Phobos are determined in Case-1 or -2.

### 2.3. Discrimination Performance

To evaluate the feasibility of the discrimination of Phobos' origin using MEGANE data and our model, we changed  $\mathbf{P}_{\text{obs}}$  within the 6-dimensional space

$[\mathbf{P}_{\min} : \mathbf{P}_{\max}]$  and investigated the origin for any  $\mathbf{P}_{\text{obs}} \in [\mathbf{P}_{\min} : \mathbf{P}_{\max}]$ . Modeled composition ranges for each element  $P_{\min,e}$  and  $P_{\max,e}$  were determined by

$$P_{\min,e} = \min_{i=0,1,2} [M_{\min,e,i}] \quad (9)$$

and

$$P_{\max,e} = \max_{i=0,1,2} [M_{\max,e,i}]. \quad (10)$$

We defined “modeled compositions” as all  $\mathbf{P}$  that can be explained by the capture and/or impact hypotheses: Case-1, -2, or -3. “Hypothesis-discriminating compositions” were also defined as  $\mathbf{P}$  that can be explained only by a unique formation hypothesis: Case-1 or -2.

To evaluate our 6-dimensional results, discrimination performance was defined as the ratio of hypothesis-discriminating compositions and modeled compositions.  $\mathcal{D}$ ,  $\mathcal{D}_{\text{cap}}$ , and  $\mathcal{D}_{\text{imp}}$  were given as

$$\mathcal{D} = \mathcal{D}_{\text{cap}} + \mathcal{D}_{\text{imp}} = \frac{n_1 + n_2}{n_1 + n_2 + n_3} \times 100 \text{ [\%]}, \quad (11)$$

$$\mathcal{D}_{\text{cap}} = \frac{n_1}{n_1 + n_2 + n_3} \times 100 \text{ [\%]}, \quad (12)$$

$$\mathcal{D}_{\text{imp}} = \frac{n_2}{n_1 + n_2 + n_3} \times 100 \text{ [\%]}, \quad (13)$$

where  $n_1$ ,  $n_2$ , and  $n_3$  were the number of data points of  $\mathbf{P}$  classified into Case-1, -2, and -3, respectively.  $\mathcal{D}$ , a sum of  $\mathcal{D}_{\text{cap}}$  and  $\mathcal{D}_{\text{imp}}$ , indicated the ratio of hypothesis discriminating compositions to modeled compositions, that is, the extent to which the formation hypothesis was discriminated within modeled compositions.  $\mathcal{D}_{\text{cap}}$  and  $\mathcal{D}_{\text{imp}}$  were the ratios of  $\mathbf{P}$  related only to the capture and impact origins, respectively.

To visualize the relationship between the compositions and origins of Phobos, we calculated the discrimination performance by 5 cases of 2-element compositions. Here the fixed two elements were pairs of Fe-, O-, Ca-, Mg-, and Th-Si, while compositions of the rest of the four elements were changed to recalculate  $n_{\text{cap}}$  and  $n_{\text{imp}}$  in Eqs. 11–13. We denoted them as  $d$ ,  $d_{\text{cap}}$ , and  $d_{\text{imp}}$  to distinguish from  $\mathcal{D}$ ,  $\mathcal{D}_{\text{cap}}$ , and  $\mathcal{D}_{\text{imp}}$ .

### 3. Results

#### 3.1. Reference Case: Modeled Asteroidal Fraction for Impact Origin of 50%

For the reference case,  $\mathcal{D}$  were calculated with varying MEGANE observation error  $E_P$  (Asteroidal fraction of 50% (reference case)’ in Table 2).  $\mathcal{D}$  was 64.7% when  $E_P = 30\%$  and it increased as  $E_P$  decreased. Throughout the calculated  $E_P$  range (0–30%),  $\mathcal{D}_{\text{cap}}$  almost agreed with  $\mathcal{D}_{\text{imp}}$ .

Here we briefly review compositional variations among end-member components (Fig. 4). As end-member compositions, Mars and asteroidal compositions

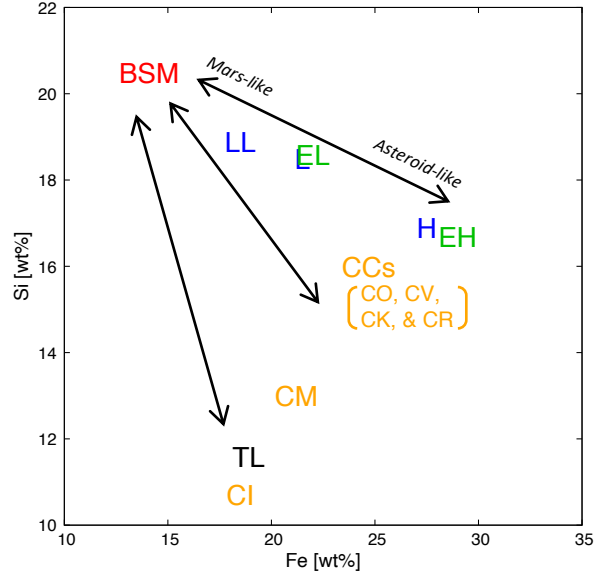


Figure 4: Variation of end-member compositions on a Fe-Si diagram (labels: Bulk Silicate Mars (BSM; red); CC (yellow); OC (blue); EC (green); and Tagish Lake (black)). End-members composition show variational extent from Mars-like composition toward asteroid-like compositions (*Mars-asteroid compositional transition*; black arrows).

are assigned as input parameters (Section 2.1.2). Since we assigned several different chondritic compositions as an input parameter, the asteroidal components (yellow, blue, green, and black labels in Fig. 4) show a more extended distribution than the Mars component (red label in Fig. 4). For convenience, a transition from Mars-like to asteroid-like compositions (black arrows in Fig. 4) will be referred to as *Mars-asteroid compositional transition* in this paper.

The relationships between 6-dimensional compositions and the corresponding origins are summarized in 2-dimensional space using  $d$ ,  $d_{\text{cap}}$ , and  $d_{\text{imp}}$  (Fig. 5).  $\mathbf{P}$  occurring beyond the asteroid-side of the Mars-asteroid compositional transition tended to have  $d_{\text{cap}}$  of 100% (yellow in Fig. 5), while those occurring beyond Mars-side of the transition had  $d_{\text{imp}}$  of 100% (blue in Fig. 5). But if  $\mathbf{P}$  occurred along the compositional transition,  $d < 100\%$ , suggesting that the formation hypothesis was not determined uniquely (gray in Fig. 5).

The extent of the modeled two-element compositions varied depending on sets of elements (Fig. 5a–e). We compared how effectively the selected pairs of two-element compositions separate the origin, by calculating the ratios between the 2-element compositions with  $d = 100\%$  (yellow, blue, and red in Fig. 5) and modeled compositions (yellow, blue, red, and gray in Fig. 5). The ratios for Fe-Si and O-Si compositions were the first and second largest among the 5 pairs, for example, 73.8 and 52.6% when  $E_P = 20\%$ , respectively, while Th-Si had the smallest value of 40.8%.

$E_P$ [%]	Asteroidal fraction of 30%			Asteroidal fraction of 50% (reference case)		
	$\mathcal{D}$ [%]	$\mathcal{D}_{\text{cap}}$ [%]	$\mathcal{D}_{\text{imp}}$ [%]	$\mathcal{D}$ [%]	$\mathcal{D}_{\text{cap}}$ [%]	$\mathcal{D}_{\text{imp}}$ [%]
30	78.3	47.4	30.9	64.7	34.4	30.2
20	87.5	52.2	35.3	73.8	39.0	34.8
10	95.4	56.6	38.9	86.6	45.3	41.3
0	99.6	52.6	47.0	95.8	45.1	50.7

$E_P$ [%]	Asteroidal fraction of 70%			Asteroidal fraction of 30–70% (practical case)		
	$\mathcal{D}$ [%]	$\mathcal{D}_{\text{cap}}$ [%]	$\mathcal{D}_{\text{imp}}$ [%]	$\mathcal{D}$ [%]	$\mathcal{D}_{\text{cap}}$ [%]	$\mathcal{D}_{\text{imp}}$ [%]
30	49.0	20.8	28.2	63.5	9.4	54.1
20	60.7	27.5	33.1	75.5	10.0	65.5
10	74.3	35.8	38.5	87.5	9.4	78.2
0	92.4	45.8	46.6	97.9	4.1	93.9

Table 2: Discrimination performances ( $\mathcal{D}$ ,  $\mathcal{D}_{\text{cap}}$ , and  $\mathcal{D}_{\text{imp}}$ ; Eqs. 14–16) calculated for modeled asteroidal fraction for impact origin of 30%, 50% (reference case), 70%, and 30–70% (practical case).

Another difference is whether the compositions that  $d = 100\%$ ,  $d_{\text{cap}} < 100\%$ , and  $d_{\text{imp}} < 100\%$  exist at the same time or not. These compositions determine the origins uniquely, although there are possibilities of either capture and impact origins (red in Fig. 5a–e). These compositions were represented only in the case of  $E_P = 0\%$ . Such compositions existed the most within Th-Si compositions and the least within Fe-Si compositions.

The populations of  $\mathbf{P}$  for Case 1–4 were distributed differently for different  $E_P$ . Discrimination performance  $\mathcal{D}$  was 64.6, 73.8, 86.6, and 95.8% when MEGANE’s error  $E_P$  was 30, 20, 10, and 0%, respectively (‘Asteroidal fraction of 50% (reference case)’ in Table 2).

### 3.2. Practical Case: Modeled Asteroidal Fraction for Impact Origin of 30–70%

Since the mixing ratio may vary by 30–70% as a function of the impact conditions, asteroidal fractions can change within that range. Here we investigated the dependency of the discrimination results on the values of asteroidal fractions.

When the modeled asteroidal fraction for the impact origin was 30%,  $\mathcal{D}$ ,  $\mathcal{D}_{\text{cap}}$ , and  $\mathcal{D}_{\text{imp}}$  were improved from the reference case. In contrast, they were reduced in the case of the modeled asteroidal fraction for the impact origin of 70% (Fig. 5; Table 2). Furthermore, the transition of  $\mathbf{P}$  for Case-2 toward Mars and asteroidal compositions were confirmed (Fig. 6a–c).

As a practical case, we also assumed the modeled asteroidal fraction of 30–70%. Under this parameter setting, it was judged as the impact origin when

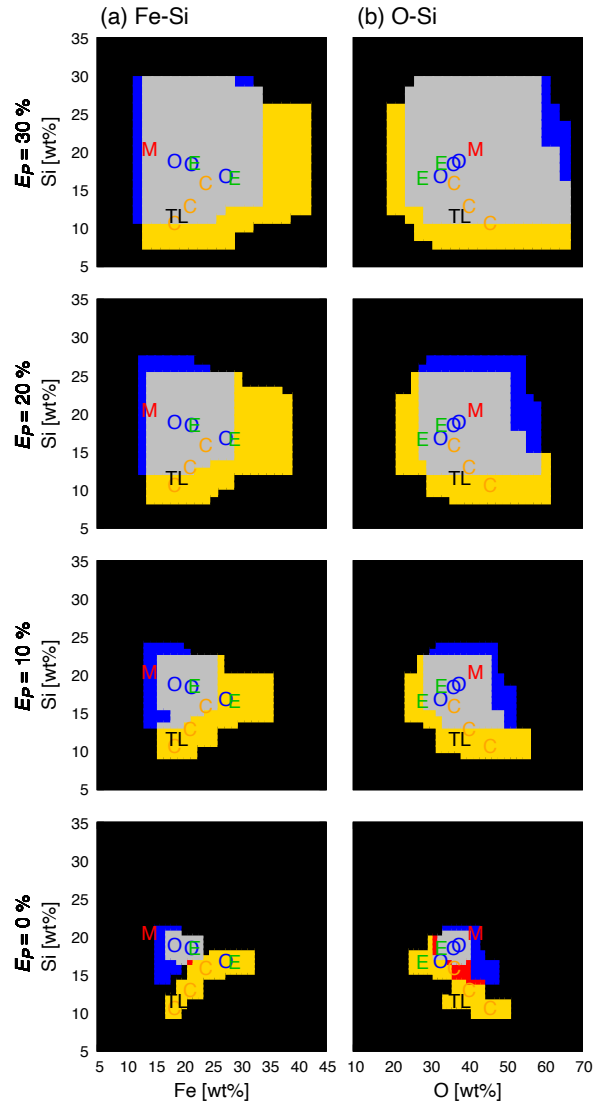
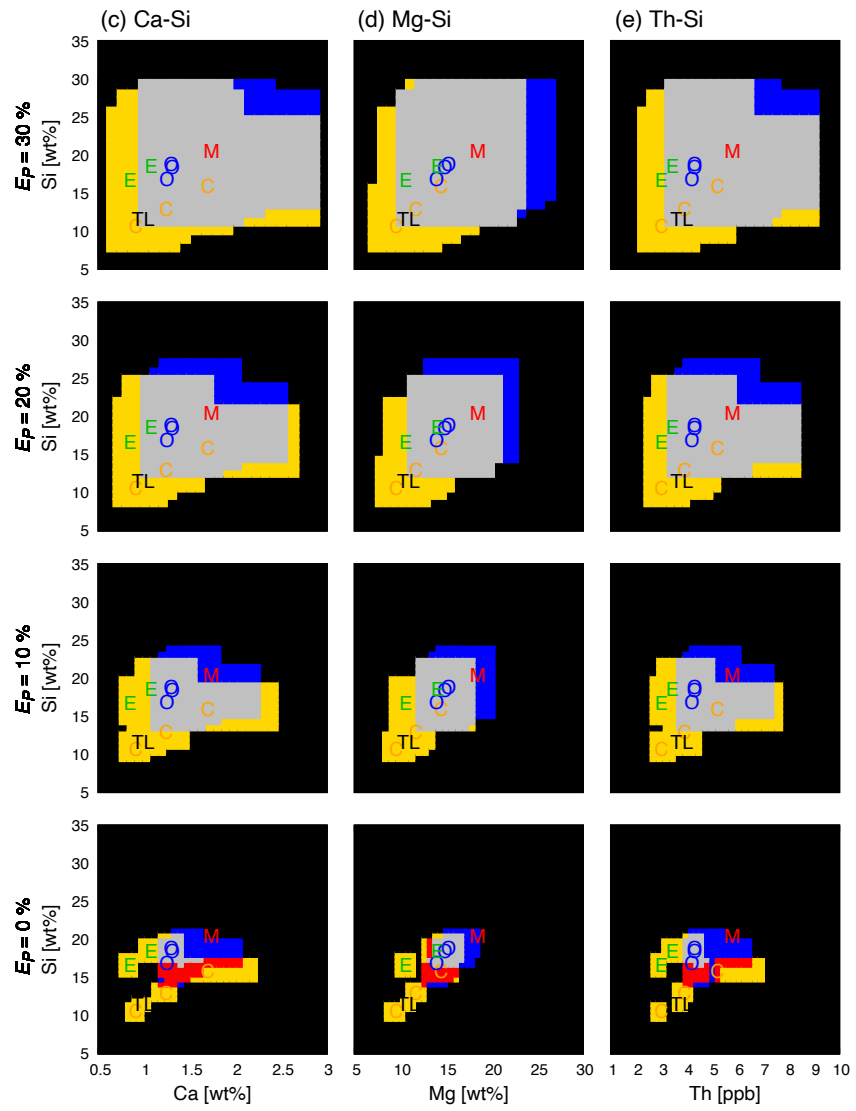


Figure 5: The relationship between 2-element compositions and the determined formation hypothesis, along with the compositional end-members (labels: Mars (“M” in red); CC (“C” in yellow); OC (“O” in blue); EC (“E” in green); and Tagish Lake (“TL” in black)). Background colors indicate whether the formation hypothesis is identified uniquely from 2-element compositions as only capture hypothesis (yellow) or only impact hypothesis (blue), is not identified uniquely from 2-element compositions but from 6- elements compositions (red), is not identified uniquely even from 6-elements composition (gray) or is explained neither by the capture nor impact hypotheses (black). (a) Fe-, (b) O-, (c) Ca-, (d) Mg-, and (e) Th-Si diagrams for varying  $E_P$  of 30, 20, 10, and 0%.





the derived mixing ratio agreed with any  $r$  between 30–70%. While  $\mathcal{D}$  had similar values to the reference case, a much larger extent of the compositions was determined as capture origin rather than impact origin (Table 2).

The distributions of  $d$  in the practical case (Fig. 6d) were similar to those in the reference case (Fig. 6b). Compared to the reference case, the whole compositions were extended, resulting from the broad compositions assumed for the impact origin.

## 4. Discussion

### 4.1. Bulk Composition of Phobos and Discrimination Performance

The inverse-solving calculations using our model revealed the relationship between the Phobos compositions measured by MEGANE and the reasonable origins. Here we discuss the relationship between the two-element compositions and the discrimination performances.

Two-element compositions had specific  $d$  values. The majority of compositions with  $d$  of 100% showed either  $d_{\text{cap}} = 100\%$  or  $d_{\text{imp}} = 100\%$  (yellow and blue, respectively, in Fig. 5). In contrast, some compositions had  $d = 100\%$ ,  $d_{\text{cap}} < 100\%$ , and  $d_{\text{imp}} < 100\%$  (red in Fig. 5) and the proportion of such two-element compositions differ among the pairs of elements (Fig. 5), with the smallest for the pair of Fe-Si. This suggests that Fe-Si compositions best discriminate the origin of Phobos when only these 6 lithophile elements are considered. Additionally, Fe-Si compositions measured by MEGANE are also expected to have the smallest errors (Lawrence et al. (2019)).

Figure 6(a) ( $E_P = 30\%$ ) shows the overall trend that  $d$  is larger when  $\mathbf{P}$  is close to end-member compositions and smaller when  $\mathbf{P}$  is an intermediate composition. However, it also shows that even if the composition completely agrees with an asteroidal composition, the origins are not always determined. For example, EL-like compositions ( $\sim 20\%$  Fe and  $\sim 19\%$  Si) can be explained by the mixture of Martian and some chondritic compositions.

### 4.2. MEGANE Error and Discrimination Performance

The discrimination performance also depends on MEGANE’s observation errors (see Section 3.1). As  $E_P$  decreased from 30% to 0%,  $\mathcal{D}$  increased from approximately 60% to more than 95% in both the reference and practical cases (Table 2). MEGANE’s instrumental performance and initial MMX operation plan estimates one-standard-deviation measurement uncertainties of 20% for Fe, Si, and Th, and 33% for O, Mg, and Ca (Lawrence et al. (2019)). In this case,  $\mathcal{D}$  is approximated to 70%, meaning that the origin will be determined from MEGANE observation in  $\sim 70\%$  of the possible cases considered in this study using only measurements of these 6 elements.

The observation errors for gamma-ray spectroscopy are strongly dependent on the total acquired measurement time and the altitude of the measurements. The relative precision of MEGANE’s measurements can be improved if the

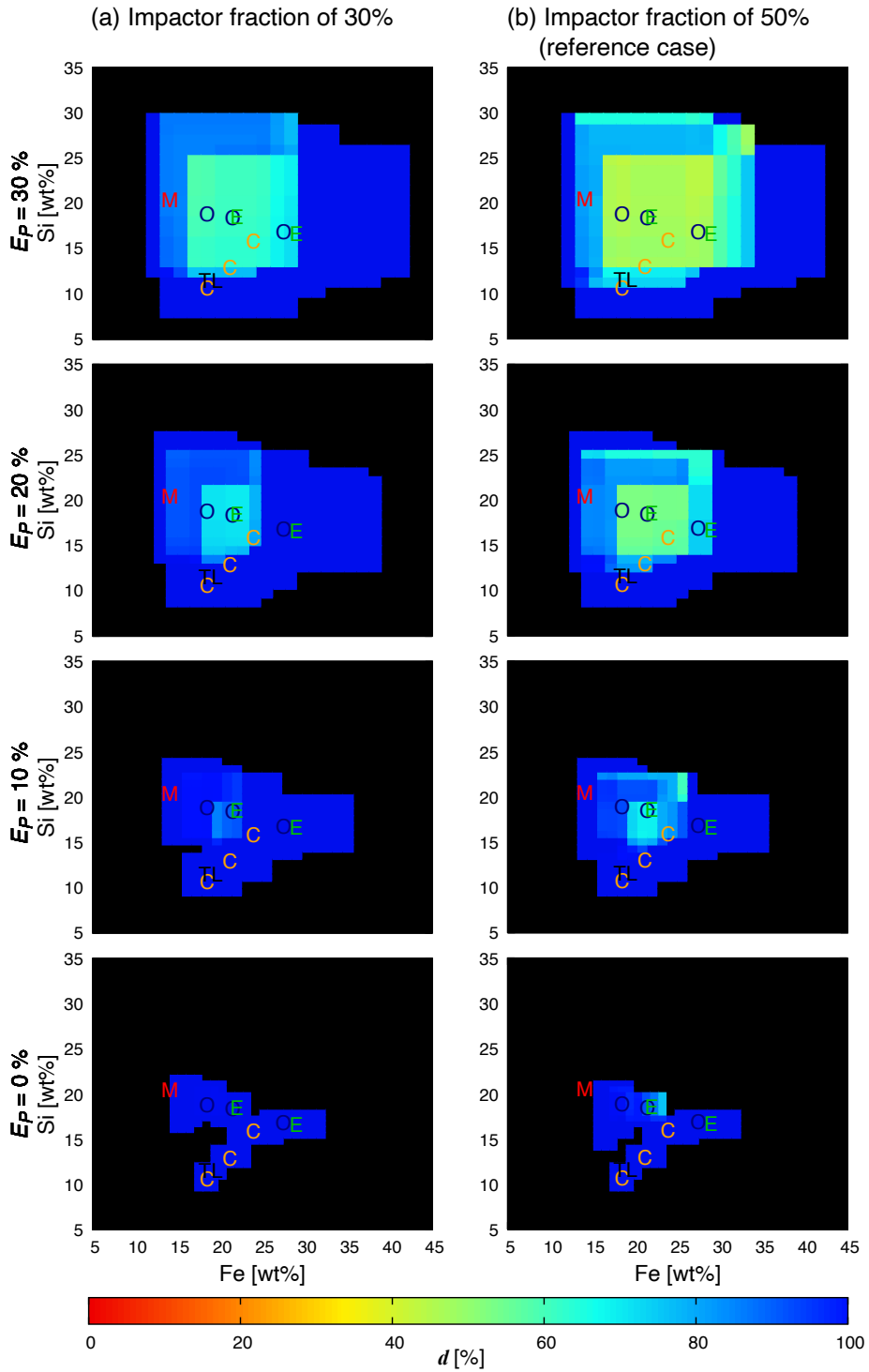
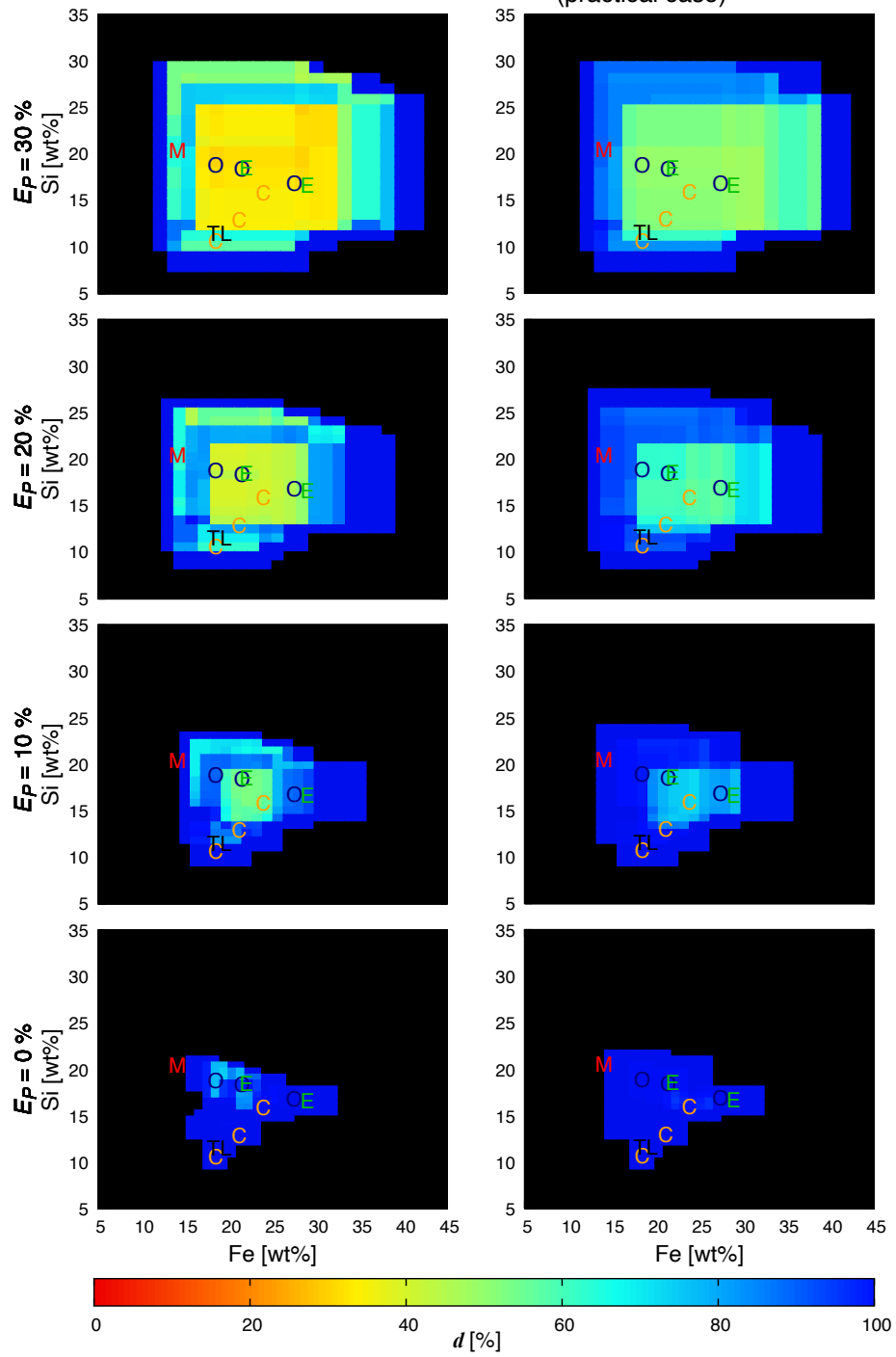


Figure 6: Discrimination performance  $d$  on Fe-Si diagrams when modeled asteroidal fraction for capture origin was 100% and for impact origin was (a) 30%, (b) 50% (reference case), (c) 70%, and (d) 30-70% (practical case), along with the compositional end-members (labels: Mars (“M” in red); CC (“C” in yellow); OC (“O” in blue); EC (“E” in green); and Tagish Lake (“TL” in black)). Note that modeled asteroidal fractions were used as criteria when judging the origin from the calculated mixing ratio (Section 2.2.2).

(c) Impactor fraction of 70%

(d) Impactor fraction of 30–70%  
(practical case)



MMX mission obtains MEGANE measurements beyond 10 days of total accumulated time at altitudes lower than the 1-body radius, under which are the conditions for which the current sensitivities were estimated (Lawrence et al. (2019); Nakamura et al. (2021)). Recently, Chabot et al. (2021) have investigated the potential footprints of MEGANE observations using the three-dimensional shape model of Phobos on the Small Body Mapping Tool (SBMT), as described in Ernst et al. (2018). They have suggested that the MEGANE data resolution from the planned MMX trajectories approximates or is coarser than the independent spectral units on Phobos. Even with the larger MEGANE error ( $E_P = 30\%$ ), more than 60% of the compositional area derived a unique solution to the formation hypothesis.

The use of additional elements will also improve discrimination performances. For example, Lawrence et al. (2019) suggested that MEGANE will measure the abundance of H, Na, K, Cl, and U in addition to the 6 elements used in this study. We specifically discuss the use of K abundance in Section 4.4.3. Since measurements of different element species have different measurement errors (Lawrence et al. (2019)), applying different errors for different elements in our model would be useful for more realistic estimates of the actual data analysis to determine the formation scenario, although the same MEGANE errors for all 6 elements were assumed in this study. The detailed MMX observation plan determined in the future will enable this model to be updated for a more specific discrimination performance.

### 4.3. Asteroid-type Classification

One of the science goals of the MMX mission is to reveal the origin of the Martian moons to understand the processes for planetary formation and material transport (Kuramoto et al. (2022)). MEGANE’s observations will help to achieve the MMX science goals and to distinguish between the capture and impact theories for Phobos’s formation. MEGANE data have the added potential to reveal the type of asteroid related to the origin as well as the formation hypothesis. Previous studies also investigated the possibilities of asteroid or meteorite type identification using gamma-ray spectroscopy data. For example, Prettyman et al. (2012) showed with analysis of gamma-ray spectroscopic data acquired by the Dawn spacecraft that there is a consistency of the composition of 4 Vesta with HED meteorites, and Peplowski et al. (2015) also investigated the similarity between asteroid 433 Eros and L- or LL-chondrite compositions.

For the quantitative evaluation, we defined classification performance  $\mathcal{C}$ ,  $\mathcal{C}_{\text{cap}}$ ,  $\mathcal{C}_{\text{imp}}$ , which were given as

$$\mathcal{C} = \frac{n'_1 + n'_2}{n_1 + n_2} \times 100 [\%], \quad (14)$$

$$\mathcal{C}_{\text{cap}} = \frac{n'_1}{n_1} \times 100 [\%], \quad (15)$$

$$\mathcal{C}_{\text{imp}} = \frac{n'_2}{n_2} \times 100 [\%]. \quad (16)$$

Note that  $n'_1$  and  $n'_2$  were the number of  $\mathbf{P}$  classified into Case-1' and -2':  $\mathbf{P}$  was explained (Case-1') by capture origin related to a unique asteroid type and (Case-2') by impact origin related to a unique impactor type.  $\mathcal{C}$  represented the ratio of  $\mathbf{P}$  which enabled the classification of asteroid type, while  $\mathcal{C}_{\text{cap}}$  and  $\mathcal{C}_{\text{imp}}$  only focused on capture and impact origins, respectively. Two-element classification performances ( $c$ ,  $c_{\text{cap}}$ , and  $c_{\text{imp}}$ ) were also calculated in the same way as described in Section 2.3.

Furthermore, final performances ( $\mathcal{F}$ ,  $\mathcal{F}_{\text{cap}}$ , and  $\mathcal{F}_{\text{imp}}$ ) were defined as

$$\mathcal{F} = \frac{\mathcal{D}}{100} \frac{\mathcal{C}}{100} \times 100 = \frac{n'_1 + n'_2}{n_1 + n_2 + n_3} \times 100 [\%], \quad (17)$$

$$\mathcal{F}_{\text{cap}} = \frac{\mathcal{D}_{\text{cap}}}{100} \frac{\mathcal{C}_{\text{cap}}}{100} \times 100 = \frac{n'_1}{n_1 + n_2 + n_3} \times 100 [\%], \quad (18)$$

$$\mathcal{F}_{\text{imp}} = \frac{\mathcal{D}_{\text{imp}}}{100} \frac{\mathcal{C}_{\text{imp}}}{100} \times 100 = \frac{n'_2}{n_1 + n_2 + n_3} \times 100 [\%]. \quad (19)$$

For the reference case,  $\mathcal{C}$  of approximately 40% was derived (Table 3) when we assumed the present-expected MEGANE error ( $E_P = 20\%$ ; Lawrence et al. (2019)), suggesting MEGANE's potential to classify the asteroid type with 40% probability when the formation hypothesis is determined, based on these 6 lithophile elements alone.  $\mathcal{C}$  improved to 42.9 and 74.9% as  $E_P$  decreased to 10 and 0%. Comparison between  $\mathcal{C}_{\text{cap}}$  and  $\mathcal{C}_{\text{imp}}$  indicates the relative difficulty to classify the asteroid type in the case of the impact origin, which appears natural considering that the mixing with Martian materials decreases the compositional variations between different compositions of asteroids. The variation of  $c$  showed a similar trend to that of  $d$ .  $c$  was larger for compositions closer to end-member compositions than for the intermediate compositions (Fig. 7a).  $c_{\text{cap}}$  and  $c_{\text{imp}}$  were larger for asteroid-like and Mars-like compositions (Figs. 7b and c).

Final performance  $\mathcal{F}$  was 37.4% when  $E_P = 20\%$ , among which  $\mathcal{F}_{\text{cap}}$  and  $\mathcal{F}_{\text{imp}}$  were 23.5 and 13.9%, respectively. When  $E_P$  was changed between 0–30%,  $\mathcal{F}_{\text{cap}}$  was always larger than  $\mathcal{F}_{\text{imp}}$  but they did not differ by a factor of 2.

In contrast to the reference case, the practical case calculation derived  $\mathcal{F}_{\text{imp}}$  larger than  $\mathcal{F}_{\text{cap}}$ . This suggests that the asteroid classification is more difficult for the capture origin than for the impact origin because the compositional variation of  $\mathbf{P}$  in the capture origin is smaller than that in the impact origin, where the uncertainty of the mixing ratio makes the compositional variation greater.

Several sets of asteroid end-members cannot be separated in the 6-element compositional spaces because some chondrite groups have similar compositions. For example, the compositions of CC groups (especially CO, CK, CV, and CR) closely resemble each other, with a slight variation in Ca and Th abundances (Table 1). Such compositional similarity can make the determination of asteroid type difficult and reduce the value of  $\mathcal{C}$ . However, our model can more efficiently discriminate the groups within CC, OS, and EC classes.

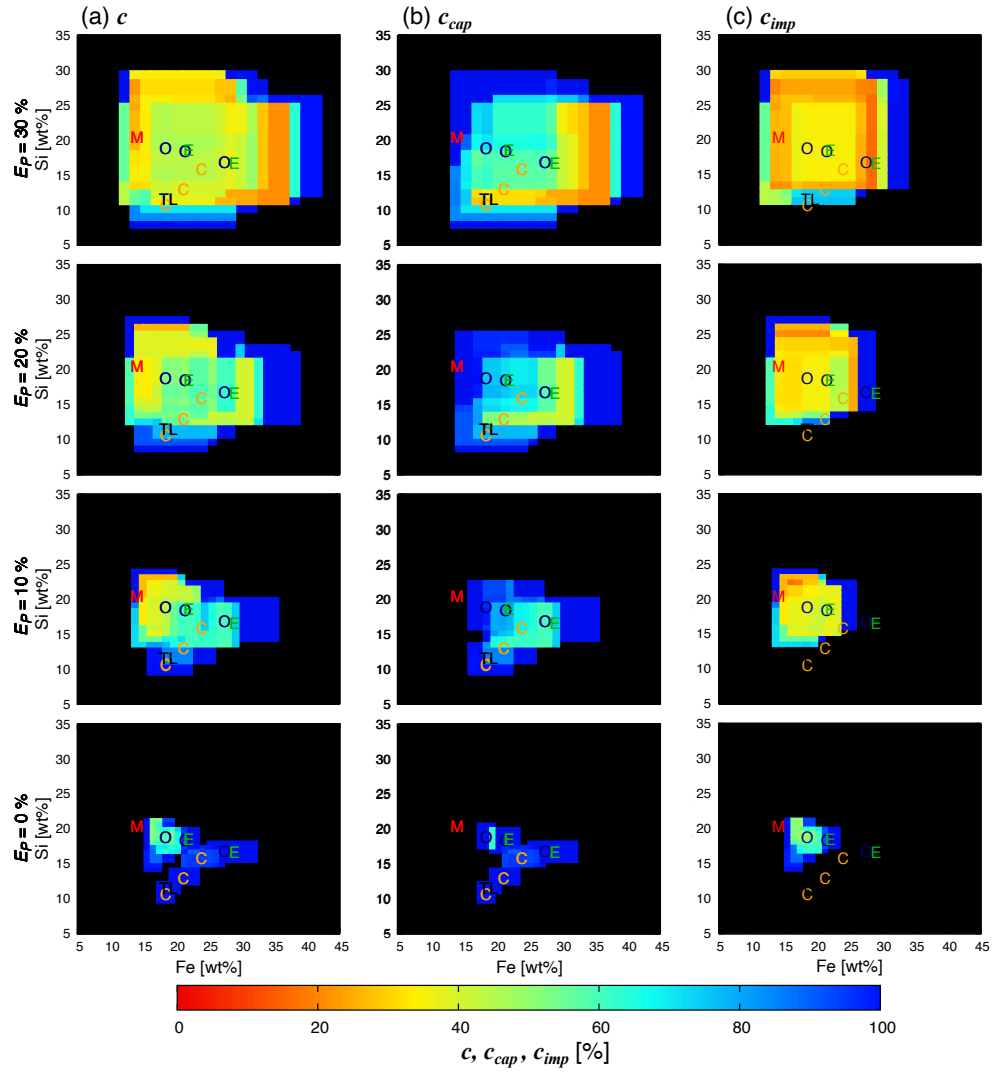


Figure 7: Classification performances (a)  $c$ , (b)  $c_{cap}$ , and (c)  $c_{imp}$  on Fe-Si diagrams when modeled asteroidal fraction for impact origin was 50% (reference case), along with end-member compositions (white label).

$E_P$ [%]	Asteroidal fraction of 50% (reference case)				Asteroidal fraction of 30–70% (practical case)			
	$\mathcal{C}$ [%]	$\mathcal{C}_{\text{cap}}$ [%]	$\mathcal{C}_{\text{imp}}$ [%]	$\mathcal{F}$ [%]	$\mathcal{C}$ [%]	$\mathcal{C}_{\text{cap}}$ [%]	$\mathcal{C}_{\text{imp}}$ [%]	$\mathcal{F}$ [%]
30	39.6	45.7	32.8	25.6	34.7	64.7	29.5	22.1
20	50.6	60.3	39.8	37.4	47.5	72.2	43.8	35.9
10	56.2	68.2	42.9	48.6	51.0	76.0	48.0	44.7
0	78.2	92.1	65.8	74.9	66.5	92.9	65.4	65.2

Table 3: Classification performances ( $\mathcal{C}$ ,  $\mathcal{C}_{\text{cap}}$ , and  $\mathcal{C}_{\text{imp}}$ ; Eqs. 14–16) calculated for modeled asteroidal fraction of 50% (reference case) and 30–70% (practical case).

#### 4.4. Limitations and Applications of the Mixing Model

##### 4.4.1. Formation scenarios not discriminated from MEGANE data

Among the 24 (12 asteroid types  $\times$  2 hypotheses) formation scenarios assumed in our model, two combinations of formation scenarios were not adequately discriminated when only considering the abundance of 6 lithophile elements: the capture of an L-type asteroid vs the impact of an EL-type asteroid; and the capture of an H-type asteroid vs the impact of an EH-type asteroid. These scenarios result in the most similar elemental compositions of Phobos in our model, especially the two scenarios in the former combination result in extremely close compositions that agree within a relative difference of  $< 3\%$ .

##### 4.4.2. Uncertainty of the Mixing Ratio

As shown in Section 3.2, discrimination performances were dependent on the modeled asteroidal fraction for the impact origin. The actual mixing ratio will be estimated from laboratory analysis such as high-precision isotopic analysis of the returned samples from Phobos (Usui et al. (2020)). However, MEGANE measurements will be performed several years before the sample analysis. Therefore, the practical model examined the results with a more realistic range of 30–70% for the mixing ratio (Hyodo et al. (2017b)) to compare the results with the reference case. Since the mixing ratio will not yet be constrained when we obtain MEGANE observation data in the future, analysis with a wide range of possibilities will be needed. The practical model can be more useful in realistic MEGANE data analysis. Therefore, MEGANE data should be revisited after the sample analysis is completed using the sample-measured mixing ratio.

##### 4.4.3. The effect of volatile loss

Volatile elements are considered key elements to discriminate the formation hypothesis because the giant impact may remove them from the impact-induced disk due to the higher temperature than the vaporization values (Hyodo et al. (2018)). For example, thermodynamic calculations by Pignatale et al. (2018) showed variations in the mineralogy of Phobos’ building blocks depending on the disk temperature. However, the effect of impact events on degassing from



impact-induced disk materials is not yet fully understood and has not been examined in detail for consistency between the Moon-forming giant impact and the volatile depletion that has been investigated throughout lunar studies (Canup et al. (2015); Charnoz et al. (2021); Charnoz & Michaut (2015); Karato (2013); Krähenbühl et al. (1973); Nakajima & Stevenson (2018); Pahlevan & Stevenson (2008); Ringwood et al. (1987); Stevenson (1987)). In this context, there should be a difference between observed volatile abundances and modeled volatile abundances for the impact origin scenario, since our mixing model does not take the preferential degassing into account. This would particularly affect K, given its volatile nature. Nevertheless, this does not mean that volatile elements are useless in our model. To demonstrate the performance of K abundances, discrimination performances were calculated using 7 elements (6 elements + K), assuming no loss of K during the impact formation process.

Adding K abundance resulted in  $\mathcal{D}$  of 74.5, 83.7, and 96.8% for  $E_P$  of 30, 20, and 10% when the modeled asteroidal fraction for the impact origin scenario was 50% (reference case). Compared with the reference case (Table 2),  $\mathcal{D}$  was improved by approximately 5–10% for any  $E_P$ .  $\mathcal{D}$  of 100% was derived for  $E_P$  of 0%, which means that the origin can be completely distinguished if we precisely know the actual 7-element compositions of Phobos. The improvement of  $\mathcal{D}$  may be because the K abundance is sensitive to the contamination of Martian material due to the large variation in K abundance between Martian and asteroidal compositions.

Considering again the uncertainty of the effect of preferential volatile loss, the more reasonable and useful application of volatile data should be a forward-solving approach. After the formation scenario is determined from the inverse-solving using the 6 elements data, the modeled volatile abundance can be predicted by the forward-solving approach. By comparing the modeled abundance with the observed abundance, the degassing ratio will be derived. This will lead to a better understanding of the giant-impact event if that is the formation origin of the Martian moons.

#### 4.4.4. *The effect of late accretion*

Because Phobos has experienced a number of impact events after its formation, exogenic materials can deposit onto Phobos’ surface as late accretion. Here we discuss the possibility to detect contamination of such exogenic materials.

A number of previous numerical studies (Hyodo et al. (2019); Hyodo & Usui (2021); Ramsley & Head (2013a); Ramsley & Head (2013b); Ramsley & Head (2017)) have suggested that Martian materials ejected from Mars by asteroidal impacts should deposit on the surface of Phobos, regardless of its origin. Thus, the returned samples acquired from the surface of Phobos by the MMX spacecraft are expected to contain these Martian materials, leading to the understanding of the habitability of Mars or providing a potential sign of life (Fujita et al. (2019); Hyodo & Usui (2021); Kurosawa et al. (2019)).

However, the concentration of Martian ejecta in Phobos regolith measurable by MEGANE is much smaller than the errors of the mixing ratio calculated with our model and much smaller than will be measurable by MEGANE. Ramsley

& Head (2013b) investigated the concentration of Martian ejecta delivered to Phobos by comparing the flux of Martian materials and that of the solar system projectile. The present concentration on the Phobos regolith was estimated at  $\sim 250$  ppm within the surface  $\sim 0.4$ m layer. Hyodo et al. (2019) updated the estimate by assuming the five largest impact craters on Mars as the source of Martian ejecta and derived a concentration of Martian ejecta and the solar system projectiles of approximately  $\sim 1000$  and  $\sim 10000$  ppm, respectively. The calculated errors were approximately 10–40% in absolute values, which is orders of magnitude larger than the concentration of Martian materials (Ramsley & Head (2013b); Hyodo et al. (2019)).

For further application, our model can be applied to the mixing of more than 2 components. In this study, we assumed the mixing of only two end-member components: BSM and a chondritic component. However, our model is also applicable to other cases, such as the mixing of several asteroid compositions or the mixing between Mars and several impactors. The former is related to the case where the parent body of the captured asteroid was formed by the impact event of different types of asteroids and the latter to the case where several types of impactors formed the impact-induced disk from which Phobos was formed.

## 5. Conclusion

This study constructed a mixing model that connected the origin of Phobos and the elemental composition that will be measured by MEGANE for 6 lithophile elements (Fe, Si, O, Ca, Mg, and Th). Forward-solving predicts the elemental composition of the surface of Phobos from a given formation scenario. Inverse-solving discriminates the origin of the Martian moons from MEGANE observation data by calculating the mixing ratio of Martian and asteroid components. The modeled performances to discriminate between formation hypotheses were calculated with varying the parameters of the mixing end-member compositions, the standard mixing ratio for the capture and impact origins, and the MEGANE observation error.

Our model shows that the ability to discriminate Phobos' origin scenario strongly depended on the MEGANE error. In a reference case, the origin was determined in 64.6% of the whole compositional area, when the MEGANE error  $E_P = 30\%$ . As the observation error decreased to 20 and 10%, the discrimination performances became larger to 73.8 and 86.6%, respectively. In the practical case, accounting for uncertainties during the impact event suggests a mixing ratio between 30 and 70% for the impact origin. In this case, MEGANE data for these 6 lithophile elements can determine the origin with 70% probability when  $E_P = 20\text{--}30\%$ , which is suggested by the initial MMX plan.

As an additional application of our model, we found that MEGANE data may also be able to help classify the type of asteroid which was captured by or impacted Mars. The classification performance was approximately 50% when  $E_P = 20\%$ , which means that when the origin is determined from the compositional measurement, the asteroid type is also determined with a probability of 50%, when these 6 lithophile elements are considered.

The use of other elements in the calculation improved the discrimination performance. For example, when we added another element K to the calculations, the performances were improved by 5–10%. Note that due to the uncertainty of possible volatile loss from an impact-induced disk, the abundance of K and other volatile elements should be used for estimates of degassing ratios as well as providing insight into Phobos' origin.

This study identified the limitation of our mixing model for certain pairs of formation scenarios; for example, the capture of an L-type asteroid and the impact of an EL-type asteroid predict indistinguishably close compositions, making it difficult for MEGANE observation to discriminate between them. However, since these groups have distinct isotopic compositions, laboratory analysis of returned samples will discriminate the origin (Fujiya et al. (2021); Usui et al. (2020)). As well as the sample collection, the MMX spacecraft will carry other scientific payloads such as a visible and near-infrared spectrometer, and a mass spectrometer (Kuramoto et al. (2022); Usui et al. (2020)). Measurements by them will provide data complementary to MEGANE data. The combination of all these observations will reduce the candidate formation scenarios, which will improve discrimination and classification performances. Observations during the MMX mission will comprehensively advance the understanding of the origin of Phobos.

## References

- Alexander, C. M. O. (2019a). Quantitative models for the elemental and isotopic fractionations in chondrites: The carbonaceous chondrites. *Geochimica et Cosmochimica Acta*, 254, 277–309. URL: <https://linkinghub.elsevier.com/retrieve/pii/S0016703719300857>. doi:10.1016/j.gca.2019.02.008.
- Alexander, C. M. O. (2019b). Quantitative models for the elemental and isotopic fractionations in the chondrites: The non-carbonaceous chondrites. *Geochimica et Cosmochimica Acta*, 254, 246–76. URL: <https://linkinghub.elsevier.com/retrieve/pii/S001670371930050X>. doi:10.1016/j.gca.2019.01.026.
- Bagheri, A., Khan, A., Efroimsky, M., Kruglyakov, M., & Giardini, D. (2021). Dynamical evidence for Phobos and Deimos as remnants of a disrupted common progenitor. *Nat Astron*, 5, 539–43. doi:10.1038/s41550-021-01306-2.
- Barucci, M. A., Reess, J.-M., Bernardi, P., Doressoundiram, A., Fornasier, S., Le Du, M., Iwata, T., Nakagawa, H., Nakamura, T., André, Y., Aoki, S., Arai, T., Baldit, E., Beck, P., Buey, J.-T., Canalias, E., Castelnau, M., Charnoz, S., Chaussidon, M., Chapron, F., Ciarletti, V., Delbo, M., Dubois, B., Gauffre, S., Gautier, T., Genda, H., Hassen-Khodja, R., Hervet, G., Hyodo, R., Imbert, C., Imamura, T., Jorda, L., Kameda, S., Kouach, D., Kouyama, T., Kuroda, T., Kurokawa, H., Lapaw, L., Lasue, J., Le Deit, L., Ledot, A., Leyrat, C., Le Ruyet, B., Matsuoka, M., Merlin, F., Miyamoto, H., Moynier, F., Nguyen Tuong, N., Ogohara, K.,

- Osawa, T., Parisot, J., Pistre, L., Quertier, B., Raymond, S. N., Rocard, F., Sakanoi, T., Sato, T. M., Sawyer, E., Tache, F., Trémolières, S., Tsuchiya, F., Vernazza, P., & Zeganadin, D. (2021). MIRS: an imaging spectrometer for the MMX mission. *Earth, Planets and Space*, *73*, 211. URL: <https://earth-planets-space.springeropen.com/articles/10.1186/s40623-021-01423-2>. doi:10.1186/s40623-021-01423-2.
- Brearley, A. J., Jones, R. H., & Papike, J. J. (1998). Chondritic meteorites. In *Planetary materials* (p. C1).
- Burns, J. A. (1978). The dynamical evolution and origin of the Martian moons. *Vistas in Astronomy*, *22*, 193–210. doi:10.1016/0083-6656(78)90015-6.
- Burns, J. A. (1992). Contradictory clues as to the origin of the Martian moons. In *Mars* (pp. 1283–301).
- Canup, R., & Salmon, J. (2018). Origin of Phobos and Deimos by the impact of a Vesta-to-Ceres sized body with Mars. *Science Advances*, *4*, eaar6887. doi:10.1126/sciadv.aar6887.
- Canup, R. M., Visscher, C., Salmon, J., & Jr, B. F. (2015). Protolunar Disk Evolution and the Depletion of Volatile Elements in the Moon. In *46th Lunar and Planetary Science Conference* (p. 2304).
- Cazenave, A., Dobrovolskis, A., & Lago, B. (1980). Evolution of the inclination of Phobos. *Nature*, *284*, 430–1. doi:10.1038/284430a0.
- Chabot, N. L., Peplowski, P. N., Ernst, C. M., Nair, H., Lucks, M., Steele, R. J., & Lawrence, D. J. (2021). MEGANE investigations of Phobos and the Small Body Mapping Tool. *Earth, Planets and Space*, *73*, 217. doi:10.1186/s40623-021-01509-x.
- Charnoz, S., & Michaut, C. (2015). Evolution of the protolunar disk: Dynamics, cooling timescale and implantation of volatiles onto the Earth. *Icarus*, *260*, 440–63. URL: <https://linkinghub.elsevier.com/retrieve/pii/S0019103515003097>. doi:10.1016/j.icarus.2015.07.018.
- Charnoz, S., Sossi, P. A., Lee, Y.-N., Siebert, J., Hyodo, R., Allibert, L., Pignatale, F. C., Landeau, M., Oza, A. V., & Moynier, F. (2021). Tidal pull of the Earth strips the proto-Moon of its volatiles. *Icarus*, *364*, 114451. doi:10.1016/j.icarus.2021.114451.
- Citron, R. I., Genda, H., & Ida, S. (2015). Formation of Phobos and Deimos via a giant impact. *Icarus*, *252*, 334–8. doi:10.1016/j.icarus.2015.02.011.
- Craddock, R. A. (1994). The origin of Phobos and Deimos. In *Lunar and Planetary Science Conference* (p. 293). volume 25.
- Craddock, R. A. (2011). Are Phobos and Deimos the result of a giant impact? *Icarus*, *211*, 1150–61. doi:10.1016/j.icarus.2010.10.023.

- DeMeo, F. E., & Carry, B. (2014). Solar System evolution from compositional mapping of the asteroid belt. *Nature*, *505*, 629–34. doi:10.1038/nature12908.
- Ernst, C. M., Barnouin, O. S., Daly, R. T., & Small Body Mapping Tool Team (2018). The Small Body Mapping Tool (SBMT) for accessing, visualizing, and analyzing spacecraft data in three dimensions. In *49th Annual Lunar and Planetary Science Conference* (p. 1043). Issue: 2083.
- Fujita, K., Kurosawa, K., Genda, H., Hyodo, R., Matsuyama, S., Yamagishi, A., Mikouchi, T., & Niihara, T. (2019). Assessment of the probability of microbial contamination for sample return from Martian moons I: departure of microbes from Martian surface. *Life Sciences in Space Research*, *23*, 73–84. Publisher: Elsevier.
- Fujiya, W., Furukawa, Y., Sugahara, H., Koike, M., Bajo, K.-i., Chabot, N. L., Miura, Y. N., Moynier, F., Russell, S. S., Tachibana, S., Takano, Y., Usui, T., & Zolensky, M. E. (2021). Analytical protocols for Phobos regolith samples returned by the Martian Moons eXploration (MMX) mission. *Earth, Planets and Space*, *73*, 1–24. URL: <https://earth-planets-space.springeropen.com/articles/10.1186/s40623-021-01438-9>. doi:10.1186/s40623-021-01438-9. Number: 1 Publisher: SpringerOpen.
- Gradie, J., & Tedesco, E. (1982). Compositional Structure of the Asteroid Belt. *Science*, *216*, 1405–7. doi:10.1126/science.216.4553.1405.
- Hahn, B. C., McLennan, S. M., Taylor, G. J., Boynton, W. V., Dohm, J. M., Finch, M. J., Hamara, D. K., Janes, D. M., Karunatillake, S., Keller, J. M., Kerry, K. E., Metzger, A. E., & Williams, R. M. S. (2007). Mars Odyssey Gamma Ray Spectrometer elemental abundances and apparent relative surface age: Implications for Martian crustal evolution. *J. Geophys. Res.*, *112*, 2006JE002821. URL: <https://agupubs.onlinelibrary.wiley.com/doi/10.1029/2006JE002821>. doi:10.1029/2006JE002821.
- Hesselbrock, A. J., & Minton, D. A. (2017). An ongoing satellite–ring cycle of Mars and the origins of Phobos and Deimos. *Nature Geoscience*, *10*, 266–9. doi:10.1038/ngeo2916.
- Hunten, M. (1979). Capture of Phobos and Deimos by Protoatmospheric Drag. *Icarus*, *37*, 113.
- Hyodo, R., Genda, H., Charnoz, S., Pignatale, F. C., & Rosenblatt, P. (2018). On the impact origin of Phobos and Deimos. IV. Volatile depletion. *The Astrophysical Journal*, *860*, 150. Publisher: IOP Publishing.
- Hyodo, R., Genda, H., Charnoz, S., & Rosenblatt, P. (2017a). On the Impact Origin of Phobos and Deimos. I. Thermodynamic and Physical Aspects. *The Astrophysical Journal*, *845*, 125. doi:10.3847/1538-4357/aa81c4.

- Hyodo, R., Genda, H., Sekiguchi, R., Madeira, G., & Charnoz, S. (2022). Challenges in Forming Phobos and Deimos Directly from a Splitting of an Ancestral Single Moon. *Planet. Sci. J.*, *3*, 204. doi:10.3847/PSJ/ac88d2. Publisher: IOP Publishing.
- Hyodo, R., Kurosawa, K., Genda, H., Usui, T., & Fujita, K. (2019). Transport of impact ejecta from Mars to its moons as a means to reveal Martian history. *Scientific Reports*, *9*, 19833. doi:10.1038/s41598-019-56139-x.
- Hyodo, R., Rosenblatt, P., Genda, H., & Charnoz, S. (2017b). On the Impact Origin of Phobos and Deimos. II. True Polar Wander and Disk Evolution. *The Astrophysical Journal*, *851*, 122. doi:10.3847/1538-4357/aa9984.
- Hyodo, R., & Usui, T. (2021). Searching for life on Mars and its moons. *Science*, *373*, 742-. doi:10.1126/science.abj1512.
- Kameda, S., Ozaki, M., Enya, K., Fuse, R., Kouyama, T., Sakatani, N., Suzuki, H., Osada, N., Kato, H., Miyamoto, H., Yamazaki, A., Nakamura, T., Okamoto, T., Ishimaru, T., Hong, P., Ishibashi, K., Takashima, T., Ishigami, R., Kuo, C.-L., Abe, S., Goda, Y., Murao, H., Fujishima, S., Aoyama, T., Hagiwara, K., Mizumoto, S., Tanaka, N., Murakami, K., Matsumoto, M., Tanaka, K., & Sakuta, H. (2021). Design of telescopic nadir imager for geomorphology (TENGOO) and observation of surface reflectance by optical chromatic imager (OROCHI) for the Martian Moons Exploration (MMX). *Earth, Planets and Space*, *73*, 218. doi:10.1186/s40623-021-01462-9.
- Karato, S.-i. (2013). Geophysical constraints on the water content of the lunar mantle and its implications for the origin of the Moon. *Earth and Planetary Science Letters*, *384*, 144–53. doi:10.1016/j.epsl.2013.10.001.
- Kawakatsu, Y., Kuramoto, K., Usui, T., Sugahara, H., Ootake, H., Yasumitsu, R., Yoshikawa, K., Mary, S., Grebenstein, M., Sawada, H., Imada, T., Shimada, T., Ogawa, K., Otsuki, M., Baba, M., Fujita, K., Zacny, K., van Dyne, D., Satoh, Y., & Tokaji, A. (2023). Preliminary design of Martian Moons eXploration (MMX). *Acta Astronautica*, *202*, 715–28. doi:10.1016/j.actaastro.2022.09.009.
- Krähenbühl, U., Ganapathy, R., Morgan, J. W., & Anders, E. (1973). Volatile elements in Apollo 16 samples: possible evidence for outgassing of the Moon. *Science*, *180*, 858–61. Publisher: American Association for the Advancement of Science.
- Kuramoto, K., Kawakatsu, Y., Fujimoto, M., Araya, A., Barucci, M. A., Genda, H., Hirata, N., Ikeda, H., Imamura, T., Helbert, J., Kameda, S., Kobayashi, M., Kusano, H., Lawrence, D. J., Matsumoto, K., Michel, P., Miyamoto, H., Morota, T., Nakagawa, H., Nakamura, T., Ogawa, K., Otake, H., Ozaki, M., Russell, S., Sasaki, S., Sawada, H., Senshu, H., Tachibana, S., Terada, N., Ulamec, S., Usui, T., Wada, K., Watanabe, S.-i., & Yokota, S.

- (2022). Martian moons exploration MMX: sample return mission to Phobos elucidating formation processes of habitable planets. *Earth, Planets and Space*, *74*, 12. URL: <https://doi.org/10.1186/s40623-021-01545-7>. doi:10.1186/s40623-021-01545-7.
- Kurosawa, K., Genda, H., Hyodo, R., Yamagishi, A., Mikouchi, T., Niihara, T., Matsuyama, S., & Fujita, K. (2019). Assessment of the probability of microbial contamination for sample return from Martian moons II: the fate of microbes on Martian moons. *Life Sciences in Space Research*, *23*, 85–100. Publisher: Elsevier.
- Lambeck, K. (1979). On the orbital evolution of the Martian satellites. *Journal of Geophysical Research*, *84*, 5651–8. doi:10.1029/JB084iB10p05651. Publisher: Wiley Online Library.
- Lawrence, D. J., Peplowski, P. N., Beck, A. W., Burks, M. T., Chabot, N. L., Cully, M. J., Elphic, R. C., Ernst, C. M., Fix, S., Goldsten, J. O., Hofer, E. M., Kusano, H., Murchie, S. L., Schratz, B. C., Usui, T., & Yokley, Z. W. (2019). Measuring the Elemental Composition of Phobos: The Mars-moon Exploration with GAMMA rays and NEUTRONS (MEGANE) Investigation for the Martian Moons eXploration (MMX) Mission. *Earth and Space Science*, *6*, 2605–23. URL: <https://onlinelibrary.wiley.com/doi/10.1029/2019EA000811>. doi:10.1029/2019EA000811.
- Murchie, S. L., Britt, D. T., Head, J. W., Pratt, S. F., Fisher, P. C., Zhukov, B. S., Kuzmin, A. A., Ksanfomality, L. V., Zharkov, A. V., Nikitin, G. E., Fanale, F. P., Blaney, D. L., Bell, J. F., & Robinson, M. S. (1991). Color heterogeneity of the surface of Phobos: Relationships to geologic features and comparison to meteorite analogs. *Journal of Geophysical Research*, *96*, 5925–45. URL: <http://doi.wiley.com/10.1029/90JB02354>. doi:10.1029/90JB02354.
- Nakajima, M., & Stevenson, D. J. (2018). Inefficient volatile loss from the Moon-forming disk: Reconciling the giant impact hypothesis and a wet Moon. *Earth and Planetary Science Letters*, *487*, 117–26. URL: <https://linkinghub.elsevier.com/retrieve/pii/S0012821X1830044X>. doi:10.1016/j.epsl.2018.01.026.
- Nakamura, T., Ikeda, H., Kouyama, T., Nakagawa, H., Kusano, H., Senshu, H., Kameda, S., Matsumoto, K., Gonzalez-Franquesa, F., Ozaki, N., Takeo, Y., Baresi, N., Oki, Y., Lawrence, D. J., Chabot, N. L., Peplowski, P. N., Barucci, M. A., Sawyer, E., Yokota, S., Terada, N., Ulamec, S., Michel, P., Kobayashi, M., Sasaki, S., Hirata, N., Wada, K., Miyamoto, H., Imamura, T., Ogawa, N., Ogawa, K., Iwata, T., Imada, T., Otake, H., Canalias, E., Lorda, L., Tardivel, S., Mary, S., Kunugi, M., Mitsuhashi, S., Doressoundiram, A., Merlin, F., Fornasier, S., Reess, J.-M., Bernardi, P., Imai, S., Ito, Y., Ishida, H., Kuramoto, K., & Kawakatsu, Y. (2021). Science operation plan of Phobos

- and Deimos from the MMX spacecraft. *Earth, Planets and Space*, 73, 227. doi:10.1186/s40623-021-01546-6.
- Pahlevan, K., & Stevenson, D. J. (2008). Equilibration After the Moon-forming Giant Impact. In *39th Annual Lunar and Planetary Science Conference* (p. 2500). Issue: 1391.
- Pajola, M., Lazzarin, M., Dalle Ore, C. M., Cruikshank, D. P., Roush, T. L., Magrin, S., Bertini, I., La Forgia, F., & Barbieri, C. (2013). PHOBOS AS A D-TYPE CAPTURED ASTEROID, SPECTRAL MODELING FROM 0.25 TO 4.0  $\mu\text{m}$ . *The Astrophysical Journal*, 777, 127. doi:10.1088/0004-637X/777/2/127.
- Pang, K. D., Pollack, J. B., Veverka, J., Lane, A. L., & Ajello, J. M. (1978). The Composition of Phobos: Evidence for Carbonaceous Chondrite Surface from Spectral Analysis. *Science*, 199, 64–6. URL: <https://www.science.org/doi/10.1126/science.199.4324.64>. doi:10.1126/science.199.4324.64.
- Pätzold, M., Andert, T., Jacobson, R., Rosenblatt, P., & Dehant, V. (2014). Phobos: Observed bulk properties. *Planetary and Space Science*, 102, 86–94. URL: <https://linkinghub.elsevier.com/retrieve/pii/S0032063314000087>. doi:10.1016/j.pss.2014.01.004.
- Peplowski, P. N. (2016). The global elemental composition of 433 Eros: First results from the NEAR gamma-ray spectrometer orbital dataset. *Planetary and Space Science*, 134, 36–51. URL: <https://linkinghub.elsevier.com/retrieve/pii/S0032063316301829>. doi:10.1016/j.pss.2016.10.006.
- Peplowski, P. N., Bazell, D., Evans, L. G., Goldsten, J. O., Lawrence, D. J., & Nittler, L. R. (2015). Hydrogen and major element concentrations on 433 Eros: Evidence for an L- or LL-chondrite-like surface composition. *Meteoritics & Planetary Science*, 50, 353–67. URL: <https://onlinelibrary.wiley.com/doi/10.1111/maps.12434>. doi:10.1111/maps.12434.
- Pignatale, F. C., Charnoz, S., Rosenblatt, P., Hyodo, R., Nakamura, T., & Genda, H. (2018). On the Impact Origin of Phobos and Deimos. III. Resulting Composition from Different Impactors. *The Astrophysical Journal*, 853, 118. doi:10.3847/1538-4357/aaa23e.
- Pollack, J. B. (1977). PHOBOS and Deimos. In *IAU Colloq. 28: Planetary Satellites* (p. 319).
- Pollack, J. B., Burns, J. A., & Tauber, M. E. (1979). Gas Drag in Primordial Circumplanetary Envelopes: A Mechanism for Satellite Capture JAMES B. POLLACK. *Icarus*, 37, 587–611.
- Pollack, J. B., Veverka, J., Pang, K., Colburn, D., Lane, A. L., & Ajello, J. M. (1978). Multicolor Observations of Phobos with the Viking Lander Cameras:



- Evidence for a Carbonaceous Chondritic Composition. *Science*, 199, 66–9. URL: <https://www.science.org/doi/10.1126/science.199.4324.66>. doi:10.1126/science.199.4324.66.
- Prettyman, T. H., Mittlefehldt, D. W., Yamashita, N., Lawrence, D. J., Beck, A. W., Feldman, W. C., McCoy, T. J., McSween, H. Y., Toplis, M. J., Titus, T. N., Tricarico, P., Reedy, R. C., Hendricks, J. S., Forni, O., Le Corre, L., Li, J.-Y., Mizzon, H., Reddy, V., Raymond, C. A., & Russell, C. T. (2012). Elemental Mapping by Dawn Reveals Exogenic H in Vesta’s Regolith. *Science*, 338, 242–6. doi:10.1126/science.1225354.
- Ramsley, K. R., & Head, J. W. (2013a). Mars impact ejecta in the regolith of Phobos: Bulk concentration and distribution. *Planetary and Space Science*, 87, 115–29. URL: <https://linkinghub.elsevier.com/retrieve/pii/S0032063313002328>. doi:10.1016/j.pss.2013.09.005.
- Ramsley, K. R., & Head, J. W. (2013b). The origin of Phobos grooves from ejecta launched from impact craters on Mars: Tests of the hypothesis. *Planetary and Space Science*, 75, 69–95. URL: <https://linkinghub.elsevier.com/retrieve/pii/S003206331200298X>. doi:10.1016/j.pss.2012.10.007.
- Ramsley, K. R., & Head, J. W. (2017). The Stickney Crater ejecta secondary impact crater spike on Phobos: Implications for the age of Stickney and the surface of Phobos. *Planetary and Space Science*, 138, 7–24. URL: <https://linkinghub.elsevier.com/retrieve/pii/S0032063315300489>. doi:10.1016/j.pss.2017.02.004.
- Ringwood, A. E., Seifert, S., & Waenke, H. (1987). A komatiite component in Apollo 16 highland breccias: Implications for the nickel-cobalt systematics and bulk composition of the Moon. *Earth and Planetary Science Letters*, 81, 105–17. Publisher: Elsevier.
- Rivkin, A. (2002). Near-Infrared Spectrophotometry of Phobos and Deimos. *Icarus*, 156, 64–75. doi:10.1006/icar.2001.6767.
- Rosenblatt, P. (2011). The origin of the Martian moons revisited. *The Astronomy and Astrophysics Review*, 19, 44. doi:10.1007/s00159-011-0044-6.
- Rosenblatt, P., Charnoz, S., Dunseath, K. M., Terao-Dunseath, M., Trinh, A., Hyodo, R., Genda, H., & Toupin, S. (2016). Accretion of Phobos and Deimos in an extended debris disc stirred by transient moons. *Nature Geoscience*, 9, 581–3. doi:10.1038/ngeo2742.
- Safronov, V. S., & Ruskol, E. L. (1977). The accumulation of satellites. *Soviet Astronomy*, 21, 211–7.
- Stevenson, D. J. (1987). Origin of the moon-The collision hypothesis. *Annual review of earth and planetary sciences*, 15, 271–315.

- Szeto, A. M. (1983). Orbital evolution and origin of the Martian satellites. *Icarus*, *55*, 133–68. doi:10.1016/0019-1035(83)90056-8.
- Taylor, G. J. (2013). The bulk composition of Mars. *Geochemistry*, *73*, 401–20. doi:10.1016/j.chemer.2013.09.006.
- Thomas, P., Veverka, J., Bell, J., Lunine, J., & Cruikshank, D. (1992). Satellites of Mars: geologic history. In *Mars* (pp. 1257–82). University of Arizona Press, Space Science Series.
- Usui, T., Bajo, K.-i., Fujiya, W., Furukawa, Y., Koike, M., Miura, Y. N., Sugahara, H., Tachibana, S., Takano, Y., & Kuramoto, K. (2020). The Importance of Phobos Sample Return for Understanding the Mars-Moon System. *Space Science Reviews*, *216*, 49. doi:10.1007/s11214-020-00668-9.